Geophys. J. Int. (2003) **152,** 443–454

Contribution of vertically travelling plane *S*-waves to dynamic and static displacements near a finite fault

Ryou Honda* and Kiyoshi Yomogida

Division of Earth and Planetary Sciences, Graduate School of Science, Hokkaido University. E-mail: ryou@eos.hokudai.ac.jp

Accepted 2002 August 19. Received 2002 April 30; in original form 2001 November 14

SUMMARY

Representing seismic waves numerically by, for example, the discrete wavenumber method, we normally decompose waves into *P-SV* and *SH* components. This scheme, however, cannot treat the exactly vertically travelling *S*-wave element (VTSE), which corresponds to $k_x = k_y = 0$, whereas VTSE exists except for a few cases of fault geometry. In order to deal with VTSE from a point source, a new *S*-wave potential must be introduced, so that its polarization is restricted on a horizontal plane. The polarization angle of VTSE is a function of the fault geometry represented by dip, rake and strike. In this study, we first point out that VTSE from a finite fault cannot be calculated even if we use the above new *S*-wave potential, because the terms originated from fault finiteness become zero if $k_x = k_y = 0$. In order to remedy this difficulty for a finite source, we define a new VTSE potential for a rectangular fault. The contribution of VTSE is large for displacements in a very low frequency range such as static displacement. The static displacement due to VTSE does not depend on a fault depth or station locations. When we take a small but finite value for k_x and k_y instead of zero, say $\delta k = 10^{-5}$, we can obtain practically accurate results even without the VTSE potential, including static displacements that have not been discussed in detail yet. Following the above scheme, accurate seismograms with both dynamic and static components can be simulated simultaneously for a fault of any configuration and station location.

Key words: finite fault model, static deformation, vertically travelling S-wave.

1 INTRODUCTION

New kinds of observations, such as kinematic GPS (e.g. Hirahara *et al.* 1996) and interferometric seismometers with laser diodes, have been recently developed, and they have the potentiality of being used as broad-band seismometers which can observe in a very low frequency range including static displacement. We are gathering data on not only elastic but also on the nonlinear behaviour of crustal deformations and making use of these new observations. If we can calculate surface displacements, including static displacement, accurately we are able to divide observed displacements into elastic and anelastic deformations. This kind of approach will play an important role in understanding crustal deformations due to earthquakes and the dynamic properties of the Earth's crust. An appropriate method to compare synthetics directly with such new observations for a realistic Earth structure is the discrete wavenumber method (Bouchon & Aki 1977; Bouchon 1979), which is ordinarily used to synthesize dynamic motions. Overcoming some difficulties, this method can calculate not only dynamic motions but also static displacement simultaneously (Honda & Yomogida 2002).

If we use the discrete wavenumber method in synthesizing seismograms, it is difficult to include static displacement. This is because of poor convergence of integration over horizontal wavenumbers for the static. Although complete displacements due to a kinematic fault model are derived in the Weyl integral, we must truncate the integration over horizontal wavenumbers when we carry out the integration numerically. To obtain seismograms, not only of dynamic motions such as *P*- and *S*-waves but also of static displacement corresponding to zero frequency, we investigated the importance of the truncation number of horizontal wavenumbers, $k_{\max}$, especially in zero and low frequency ranges (Honda & Yomogida 2000, 2002). In the case of a homogeneous half space, Honda & Yomogida (2002) concluded that 4 km^{-1} is a suitable value for the truncation number of horizontal wavenumbers to calculate surface displacements including accurate static displacement.

In addition to the difficulty related to the truncation number of the wavenumber integration, there is another problem in obtaining accurate seismograms inherent to any method based on the plane-wave decomposition. We normally decompose waves into *P-SV* and *SH* coordinates.

*Now at: Institute of Seismology and Volcanology, Graduate School of Science, Hokkaido University, North 10 West 8, Kita-ku, Sapporo 060-0810, Japan.

This decoupling has the essential singularity if both of horizontal wavenumbers k_x and k_y are to be zero, because *SV*- and *SH*-wave potentials become zero. This wave corresponds to a vertically travelling plane *S*-wave (VTSE). This component is important for obtaining accurate surface displacement particularly for the static component, as shown later. For a point source, Takenaka (1990) and Hirata (1992) introduced a new coordinate system in order to remove this singularity. Hirata (1992) studied the effect of VTSE radiated from a point source on seismic waveforms. Comparing displacement waveforms with and without VTSE, he pointed out the effect of VTSE is more noticeable in a low frequency range. But he did not check this effect in a finite fault case and did not deal carefully with the static component.

In this study, we shall show that VTSE cannot be dealt exactly for a finite source in the same manner as that for a point source because of an additional singularity in the formulation related to fault finiteness. The terms originated from the fault finiteness become zero as horizontal wavenumbers k_x and k_y go to zero. We will develop a new scheme to avoid this type of singularity for a finite fault and investigate the degree of the contribution of VTSE to surface displacements in order to obtain accurate seismograms with the discrete wavenumber method. Although we follow the discrete wavenumber method, the basic concept of this study is valid for any other approaches based on the plane-wave decomposition.

2 POTENTIALS FOR A POINT SOURCE

Let us first consider *P*-, *SV*- and *SH*-wave displacement potentials radiated from a coupled point source in the discrete wavenumber representation (e.g. Honda & Yomogida 1999). Using *SV*- and *SH*-potentials, the displacement vector is written by

$$\tilde{U} = \nabla\phi + \nabla \times (0, 0, \psi_{SH}) + \nabla \times \nabla \times (0, 0, \psi_{SV}) \tag{1}$$

(e.g. Aki & Richards 1980). x and y correspond to the NS and EW directions, respectively (Fig. 1). Potentials for *P*-, *SV*- and *SH*-waves at a reference point (x_o, y_o, z_o) in the Cartesian coordinate are

$$\phi_{\pm} = \frac{i M_o}{8\pi^2 \mu k_\beta^2} \int_{-\infty}^{\infty}\int_{-\infty}^{\infty} A_{\pm} \exp i(k_x(x - x_o) + k_y(y - y_o) \mp \nu(z - z_o))\, dk_x dk_y, \tag{2}$$

$$\psi_{SV\pm} = \frac{i M_o}{8\pi^2 \mu k_\beta^2} \int_{-\infty}^{\infty}\int_{-\infty}^{\infty} B_{sv\pm} \exp i(k_x(x - x_o) + k_y(y - y_o) \mp \gamma(z - z_o))\, dk_x dk_y, \tag{3}$$

$$\psi_{SH\pm} = \frac{i M_o}{8\pi^2 \mu k_r^2} \int_{-\infty}^{\infty}\int_{-\infty}^{\infty} B_{sh\pm} \exp i(k_x(x - x_o) + k_y(y - y_o) \mp \gamma(z - z_o))\, dk_x dk_y, \tag{4}$$

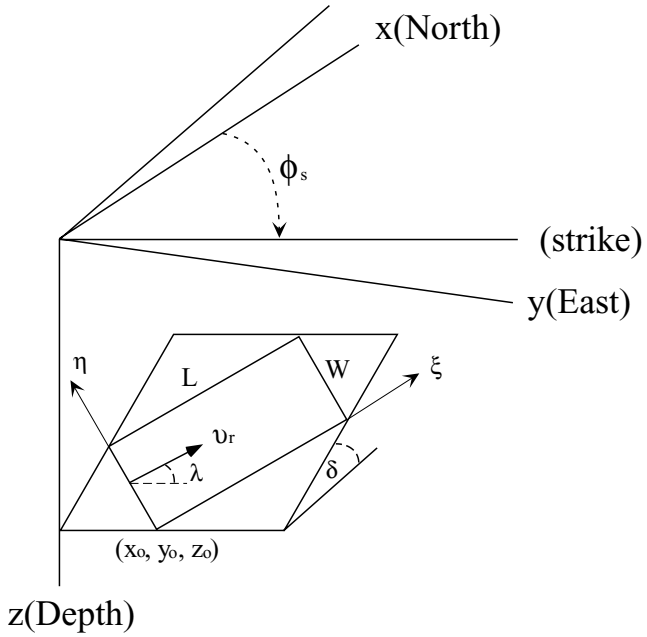

Figure 1. Fault geometry. L, W, ϕ_s, δ and λ are length, width, strike, dip and rake of the fault, respectively, whose definitions are after Aki & Richards (1980).

where

$$A_{\pm} = -\frac{k_x^2}{\nu} M_{xx} - \frac{2k_x k_y}{\nu} M_{xy} \pm 2k_x M_{xz} - \frac{k_y^2}{\nu} M_{yy} \pm 2k_y M_{yz} - \nu M_{zz}, \tag{5}$$

$$B_{sv\pm} = \mp \frac{k_x^2}{k_r} M_{xx} \mp \frac{2k_x k_y}{k_r} M_{xy} + \frac{k_x \left(k_\beta^2 - 2k_r^2\right)}{\gamma k_r} M_{xz} \mp \frac{k_y^2}{k_r} M_{yy} + \frac{k_y \left(k_\beta^2 - 2k_r^2\right)}{\gamma k_r} M_{yz} \pm k_r M_{zz}, \tag{6}$$

$$B_{sh\pm} = -\frac{k_x k_y}{\gamma} M_{xx} + \frac{k_x^2 - k_y^2}{\gamma} M_{xy} \pm k_y M_{xz} + \frac{k_x k_y}{\gamma} M_{yy} \mp k_x M_{yz}, \tag{7}$$

with the seismic moment M_o and moment tensors related to fault parameters ϕ_s, δ and λ (see Box 4.4 of Aki & Richards 1980 p. 117, or Fig. 1). k_r is the horizontal wavenumber, $k_r^2 = k_x^2 + k_y^2$, and k_β is for S-wave. ν and γ are so understood as $\nu^2 = k_\alpha^2 - k_r^2$ and $\gamma = k_\beta^2 - k_r^2$. The subscript plus and minus signs in the above equations correspond to upward and downward propagating potentials, respectively.

Surface displacements by P- and SV-waves are given by

$$U_{r'} = \frac{\partial \phi_\pm}{\partial r'} - \frac{\partial \psi_{SV_\pm}}{\partial z}, \tag{8}$$

$$W = \frac{\partial \phi_\pm}{\partial z} + \frac{\partial \psi_{SV_\pm}}{\partial r'}, \tag{9}$$

where U_r is the r' component (direction of the wave propagation shown in Fig. 2) of surface displacement and W is the vertical. The surface displacement by SH-waves, which is horizontal and perpendicular to $U_{r'}$, is given by

$$V_\theta = -\frac{\partial \psi_{SH_\pm}}{\partial r'}. \tag{10}$$

In the case of $k_r \neq 0$, N–S and E–W displacements U_x and V_y are obtained by

$$U_x = \frac{k_x}{k_r} U_{r'} - \frac{k_y}{k_r} V_\theta, \tag{11}$$

$$V_y = \frac{k_y}{k_r} U_{r'} + \frac{k_x}{k_r} V_\theta, \tag{12}$$

Although the above formulations can be easily extended to a layered medium using the reflection-matrix method (Kennett & Kerry 1979; Luco & Apsel 1983), all the displacements obtained from SV- and SH-potentials vanish in the case of $k_x = k_y = 0$. This type of waves correspond to VTSE, even though VTSE exists except a few special cases. We shall call this type of difficulty 'the singularity of VTSE'. In the following section, we shall introduce a new S-wave potential in order to avoid this singularity, following an approach developed by Hirata (1992) for a point source.

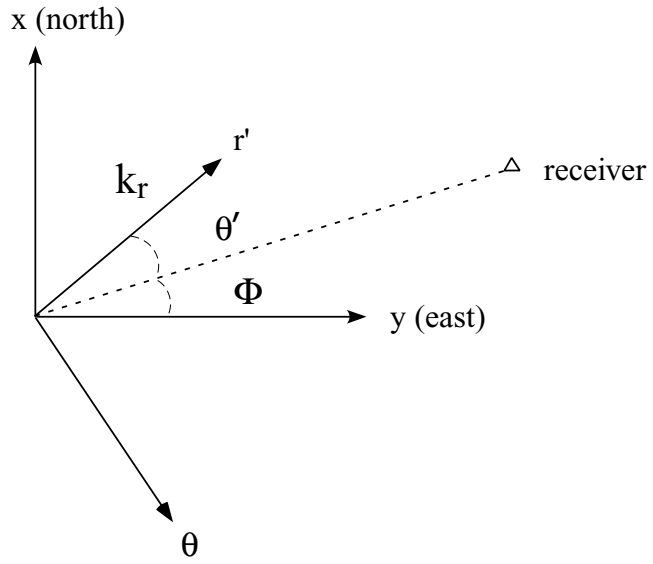

Figure 2. Relation between horizontal wavenumber k_r and receiver direction in the cylindrical coordinate.

3 INTRODUCTION OF VTSE POTENTIAL

3.1 Representation of exact VTSE

Initally, we decompose three components of *S*-wave displacement potential $\tilde{\psi}$ into *SV*- and *SH*-wave displacement potentials, as shown in eqs (3) and (4). This decomposition, however, cannot accurately deal with a vertically travelling plane *S*-wave element with $k_x = k_y = 0$, because *SH*- and *SV*-wave potentials are not distinguishable in this case and the displacements expressed by *SV*- and *SH*-waves with (3) and (4) become zero. This problem has been recognized as the difficulty of a vertical plane *S*-wave incidence (e.g. Horike *et al.* 1990; Ohori *et al.* 1992; Uebayashi *et al.* 1992). We first briefly review previous approaches in order to distinguish the singularity for a point source from that for a finite fault to be discussed in the next section.

Although Takenaka (1990) and Ohori *et al.* (1992) introduced special potentials in order to represent VTSE, they were interested only in the effect of layered media and did not consider the singularity related to a seismic source. On the other hand, Hirata (1992) carefully studied the effect of VTSE from a point source and presented formulations due to VTSE from a finite fault in a formal manner. Following Hirata (1992), we introduce a new coordinate system (x', y') in the case of a horizontal wavenumber to be zero for VTSE (Fig. 3). The particle motion of VTSE should be confined on a horizontal plane, which is defined by θ_s. θ_s depends only on the fault geometry, in terms of δ, λ and ϕ_s in Fig. 1:

$$\tan\theta_s = \frac{V_y}{U_x} = -\frac{\psi_x}{\psi_y},$$

$$= \frac{\cos\delta\cos\lambda\sin\phi_s - \cos 2\delta\sin\lambda\cos\phi_s}{\cos\delta\cos\lambda\cos\phi_s + \cos 2\delta\sin\lambda\sin\phi_s}. \tag{13}$$

The *S*-wave polarization angle defined by (13) cannot be determined for either a vertical strike-slip fault ($\delta = 90^\circ$ and $\lambda = 0^\circ, \pm 180^\circ$) or a 45° dip-slip fault ($\delta = 45^\circ$ and $\lambda = \pm 90^\circ$). Since an amplitude of VTSE becomes zero in these cases, it is not necessary to consider the effect of VTSE. We then express vertically upward and downward travelling *S*-wave displacement potentials, ψ_+ and ψ_-, for VTSE as

$$\psi_\pm = -\psi_{x\pm}\sin\theta_s + \psi_{y\pm}\cos\theta_s, \tag{14}$$

$$= \frac{iD}{2L_xL_yk_\beta\mu}(M_{yz}\sin\theta_s + M_{xz}\cos\theta_s)\exp(\mp i\gamma(z - z_o)), \tag{15}$$

where $\psi_{x\pm}$ and $\psi_{y\pm}$ are the displacement potentials with zero horizontal wavenumber for x and y directions. D is the amount of slip. L_x and L_y are the charateristic length of x and y directions for the discretization. Note that $\psi_\pm$ are functions of neither x' nor y' but only z. This represent the VTSE potential for a point source.

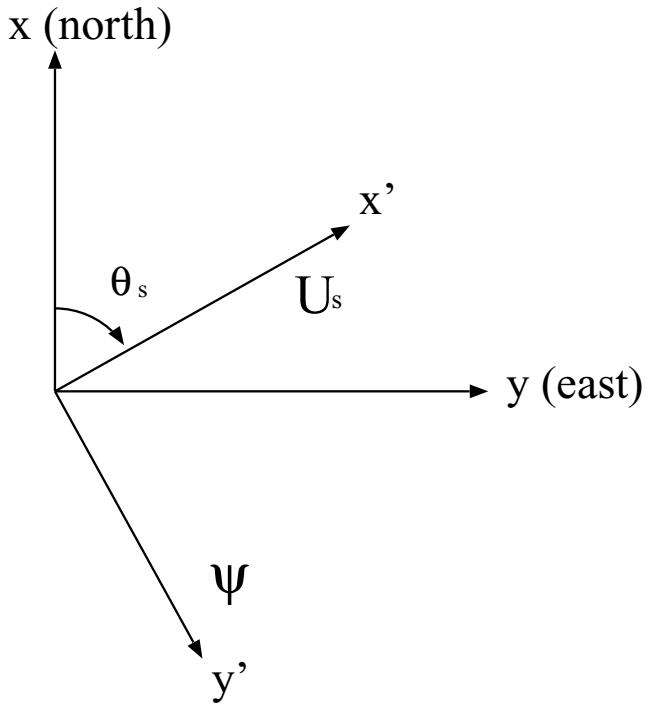

Figure 3. Relation between two horizontal components of a *S*-wave vector potential ψ and *S*-wave displacements U_s. θ_s is the polarization angle of *S*-wave due to a vertically travelling plane *S*-wave element (VTSE).

The displacement related to VTSE has x' component only, and is represented by

$$\tilde{U}_{s\pm} = \left(\frac{\partial}{\partial x'}, \frac{\partial}{\partial y'}, \frac{\partial}{\partial z}\right) \times (0, \psi_{\pm}, 0) = \left(-\frac{\partial \psi_{\pm}}{\partial z}, 0, 0\right). \tag{16}$$

To extend this approach to a layered medium, we define a standard displacement-stress matrix for VTSE expressed by

$$\begin{cases} U_{s\pm} = (-i\gamma \; i\gamma) \begin{pmatrix} \psi_- \\ \psi_+ \end{pmatrix}, \\ \sigma_{zy'} = \mu \left(\frac{\partial U_s}{\partial z} + \frac{\partial U_s}{\partial y'}\right) = (\mu\gamma^2 \; \mu\gamma^2) \begin{pmatrix} \psi_- \\ \psi_+ \end{pmatrix}. \end{cases} \tag{17}$$

The formulations (17) look similar to those of *SH* wave. This means that we can calculate VTSE directly, only replacing a standard matrix for *SH* wave by that of VTSE in the (x', y') coordinate system (i.e. U_s and $\sigma_{zy'}$).

Although we represent displacement potentials in the Cartesian coordinate, it is natural to use a cylindrical coordinate system for a point source. Using (15), we can calculate also VTSE in a cylindrical coordinate case, as shown in the Appendix. Even if potentials are represented in the cylindrical coordinate, surface displacements are obtained through (8)–(10). As a result, we can see displacements due to *SV*- and *SH*-waves vanish in the case of $k_r = 0$. That is, VTSE can be included easily in the cylindrical coordinate case, applying the VTSE potential derived in this section (i.e. eq. 15) with L replacing L_x and L_y, as shown in Bouchon (1981).

3.2 Reflection coefficient of the VTSE potential at the free surface

Since we represent VTSE in the formulation of the potential (15), the reflection coefficient at the free surface is different from that of *SH* wave. Assuming a plane *S*-wave incidence to an interface at $z = 0$, incident and reflected waves are represented as follows:

$$\psi_{\text{inc}} = C_{\text{inc}} \exp i(k_x(x - x_o) + k_y(y - y_o) - \gamma(z - z_o)), \tag{18}$$

$$\psi_{\text{ref}} = C_{\text{ref}} \exp i(k_x(x - x_o) + k_y(y - y_o) + \gamma(z + z_o)), \tag{19}$$

where C_{inc} and C_{ref} are the amplitudes of the incident and reflected waves . Referring eqs (16) and (17), the displacement due to VTSE is obtained by

$$U_s = -\left(\frac{\partial \psi_{\text{inc}}}{\partial z} + \frac{\partial \psi_{\text{ref}}}{\partial z}\right) \tag{20}$$

$$= -(-i\gamma C_{\text{inc}} \exp i(-\gamma z) + i\gamma C_{\text{ref}} \exp i\gamma z) \exp i(k_x(x - x_o) + k_y(y - y_o) + \gamma z_o). \tag{21}$$

Considering the boundary condition at the free surface,

$$\sigma_{zy'} = \mu \frac{\partial U_s}{\partial z}\bigg|_{z=0} = \mu\gamma^2(C_{\text{inc}} + C_{\text{ref}}) \exp i(k_x(x - x_o) + k_y(y - y_o) + \gamma z_o), \tag{22}$$

$$= 0. \tag{23}$$

As a result, we obtain the reflection coefficient of VTSE at the free surface to be $\frac{C_{\text{ref}}}{C_{\text{inc}}} = -1$. Note that if VTSE is not dealt in the potential form but in a displacement form, the coefficient is the same as the SH case. Making use of $\psi_{\pm}$ in (15) and a *P*-wave potential $\phi_{\pm}$, we can calculate all the components of seismograms even for VTSE or $k_x = k_y = 0$. NS and EW components of displacements are finally obtained by

$$U_x = U_s \cos\theta_s, \tag{24}$$

$$V_y = U_s \sin\theta_s. \tag{25}$$

Following the above procedure, we can obtain VTSE surface displacements for a point source in any coordinate system.

4 POTENTIALS FOR A FINITE FAULT

Since our interest is surface displacement near a realistic fault, we shall introduce potentials for a finite fault by the integration of point source potentials (2) ∼ (4) over the whole fault plane. After we extend the above equations into such a finite fault case, we find an additional singularity related to the fault finiteness. In order to understand this additional singularity, let us first introduce potentials for a finite source. As shown in Fig. 1, we assume a unilateral and unidirectional rupture propagation. ξ represents the direction of rupture propagating and η is the other direction of the fault segment. Using the transformation matrix of coordinate systems

$$\begin{pmatrix} C_{11} & C_{12} & C_{13} \\ C_{21} & C_{22} & C_{23} \\ C_{31} & C_{32} & C_{33} \end{pmatrix} = \begin{pmatrix} \sin\phi_s \cos\delta \cos\lambda - \cos\phi_s \sin\lambda & \sin\phi_s \cos\delta \sin\lambda + \cos\phi_s \cos\lambda & \sin\phi_s \sin\delta \\ -\cos\phi_s \cos\delta \cos\lambda - \sin\lambda \sin\phi_s & -\cos\phi_s \cos\delta \sin\lambda + \sin\phi_s \cos\lambda & -\cos\phi_s \sin\delta \\ -\sin\delta \cos\lambda & -\sin\delta \sin\lambda & \cos\delta \end{pmatrix}.$$

where ϕ_s, λ and δ represent strike, rake and dip angles, respectively, we can express a position on the fault (x_o, y_o, z_o) as

$$\begin{pmatrix} x \\ y \\ z \end{pmatrix} = \begin{pmatrix} C_{11} & C_{12} & C_{13} \\ C_{21} & C_{22} & C_{23} \\ C_{31} & C_{32} & C_{33} \end{pmatrix} \begin{pmatrix} \eta \\ \xi \\ 0 \end{pmatrix} + \begin{pmatrix} x_o \\ y_o \\ z_o \end{pmatrix}.$$

After the above operation, we integrate the point-source potentials of (2)–(4) to obtain potentials for a finite fault with length L and width W as follows:

$$\int_0^L \int_0^W \exp i \left(\frac{\omega}{v_r} \xi - k_x(C_{11}\eta + C_{12}\xi) - k_y(C_{21}\eta + C_{22}\xi) \pm \nu(C_{31}\eta + C_{32}\xi) \right) d\eta\, d\xi.$$

It leads to the following expressions of finite-fault potentials:

$$\phi_\pm = \frac{iD}{2L_x L_y k_\beta^2} A_\pm I_L I_W \exp i(k_x(x - x_o) + k_y(y - y_o) \mp \nu(z - z_o)) \equiv C_{P\pm} \exp(\mp i \nu z) \tag{26}$$

$$\psi_{SV\pm} = \frac{iD}{2L_x L_y k_\beta^2} B_{sv\pm} I_L I_W \exp i(k_x(x - x_o) + k_y(y - y_o) \mp \gamma(z - z_o)) \equiv C_{SV\pm} \exp(\mp i \gamma z), \tag{27}$$

$$\psi_{SH\pm} = \frac{iD}{2L_x L_y k_r^2} B_{sh\pm} I_L I_W \exp i(k_x(x - x_o) + k_y(y - y_o) \mp \gamma(z - z_o)) \equiv C_{SH\pm} \exp(\mp i \gamma z), \tag{28}$$

where

$$k_x = \frac{2\pi}{L_x} n_x, \quad k_y = \frac{2\pi}{L_y} n_y,$$

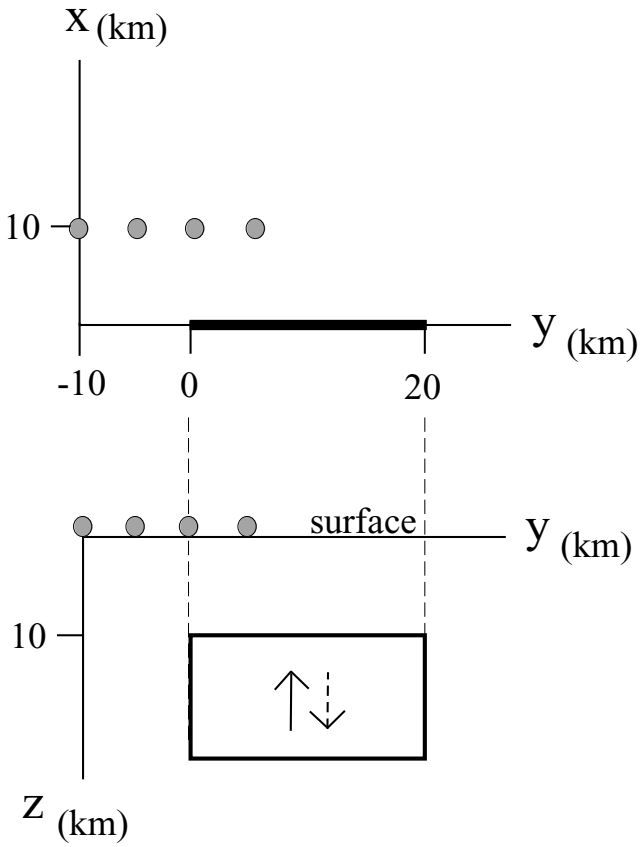

Figure 4. Station locations at surface for Figs 5, 7 and 8. Circles show stations and a fat line show the fault projection to surface and x-z plane.

Table 1. Fault parameters for the model in Fig. 4.

Fault length (strike)	20 km
Fault width (down-dip)	10 km
Depth of the fault top	30 km, 10 km and 100 m
Slip on the fault	2 m
Dip angle δ	90°
Strike ϕ_s	90°
Rake λ	90° (dip-slip)
Rupture velocity	2.5 km s^{-1}
Reference point (x_o, y_o)	(0, 0)

$$I_L \equiv \frac{\exp i L(\omega/v_r - C_{12}k_x - C_{22}k_y \pm C_{32}\Lambda) - 1}{(\omega/v_r - C_{12}k_x - C_{22}k_y \pm C_{32}\Lambda)i}\,, \tag{29}$$

$$I_W \equiv \frac{\exp i W(-C_{11}k_x - C_{21}k_y \pm C_{31}\Lambda) - 1}{(-C_{11}k_x - C_{21}k_y \pm C_{31}\Lambda)i}\,, \tag{30}$$

Λ is the vertical wavenumber (i.e. ν for *P*-waves or γ for *S*-waves).

5 SINGULARITY DUE TO VTSE FOR A FINITE FAULT

In the previous two sections, we reviewed VTSE potential for both a point source and a finite fault. Now let us observe how a new singularity appear in the VTSE potential for a finite fault. Setting $k_x = k_y = 0$ in (29) and (30), we see that potentials become zero in some cases. For example, substituting $\pm 90^\circ$ for λ, that is, a dip-slip fault, C_{31} become zero. I_W in (26)–(28) cannot be determined when horizontal wavenumbers are zero. For potentials in the cylindrical coordinate, we introduce a simple example in the appendix and show that the singularity for such a circular fault does not exist. We can obtain accurate displacement with the VTSE potential (15) directly multiplied by the above finiteness terms in the cylindrical coordinate system.

We must develop a new approach to solve the above singularity problem inherent to a finite fault in the Cartesian coordinate. We shall show analytical and numerical methods to avoid this singularity. In order to avoid the singularity for a finite fault analytically, we may introduce asymptotic solutions for I_L and I_W with very small denominators, as follows:

$$I_L \equiv \frac{\exp i L\epsilon - 1}{i\epsilon} \sim L \quad (\epsilon = \omega/v_r - C_{12}k_x - C_{22}k_y \pm C_{32}\Lambda \ll 1)\,, \tag{31}$$

$$I_W \equiv \frac{\exp i W\epsilon - 1}{i\epsilon} \sim W \quad (\epsilon = -C_{11}k_x - C_{21}k_y \pm C_{31}\Lambda \ll 1)\,. \tag{32}$$

Multiplying the *S*-wave potential (15) by (31) and (32), we can deal with VTSE from a finite fault directly.

The analytical approach is exact, but in order to obtain practically accurate seismograms for a finite fault, we recommend the following numerical device because this procedure can be easily implemented in the discrete wavenumber algorithm. We give a small but finite number to horizontal wavenumbers, k_x and k_y, instead of zero to avoid the singularity, for example,

$$k_x = \frac{2\pi}{L_x}n \quad (n \neq 0)\,, \tag{33}$$

$$= \delta k \quad (n = 0)\,, \tag{34}$$

so as for k_y. Hereafter, we call these waves with a small horizontal wavenumber δk approximated VTSE and waves represented by eqs (15), (31) and (32) exact VTSE.

In order to confirm the accuracy of seismograms and estimate the effect of VTSE for a finite fault, we synthesize seismograms in the following example. We calculate surface displacements in a homogeneous half-space for a vertical dip-slip fault whose top is 10 km deep and stations locations shown in Fig. 4. The fault is 20 km long and 10 km wide. Details of fault parameters are listed in Table 1. *P*- and *S*-wave velocities are 5.6 and 3.2 km s^{-1}, respectively.

At first, we estimate a reasonable value of δk to replace zero. Hirata (1992) used such finite values of k_x and k_y, but as small as $\delta k = 10^{-15}$ for a point source. He showed that even such a small value of δk does not give accurate synthetic seismograms. Uebayashi *et al.* (1992) calculated seismic motions due to a rectangular fault in 3-D sedimentary basin, using $\delta k = 10^{-3}$ instead of zero without checking whether it is the appropriate value or not, particularly for a very low frequency in which the effect of VTSE is strong. Fig. 5 compares seismograms with $\delta k = 10^{-5}$ as approximated VTSE with those with exact VTSE, observed at a station $(x, y) = (10, -10)$ in Fig. 4. Both seismograms are virtually identical and their static displacements agree very well with an analytical solution of Okada (1985) represented by broken lines.

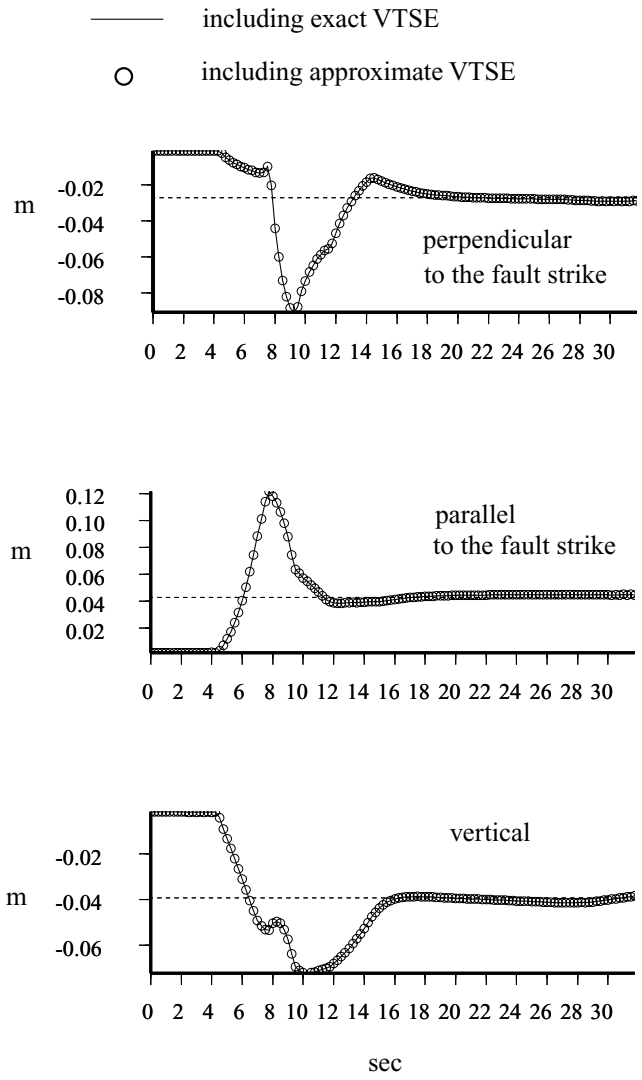

Figure 5. Comparison between synthetic seismograms including exact VTSE and approximate VTSE, that is, using finite value $\delta k = 10^{-5}$, at station $x = 10$, $y = -10$ in Fig. 4. Dotted lines are static displacements obtained by Okada's analytical solutions. Slid lines are synthesized seismograms by using a *S*-wave potential (15), that is, exact VTSE and circles are those with approximate VTSE.

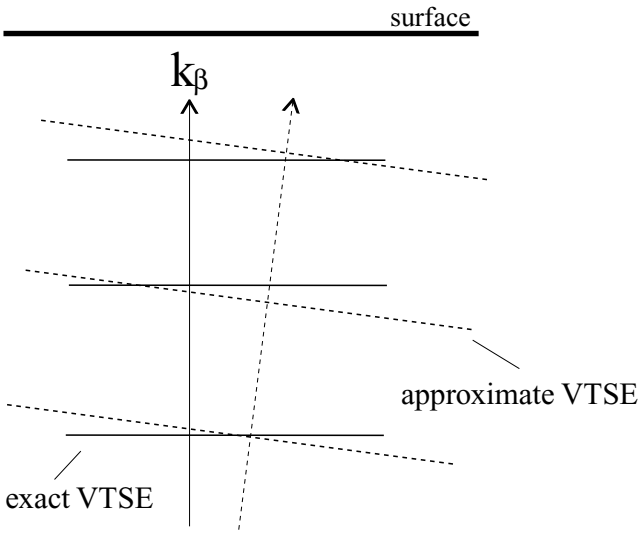

Figure 6. Schematic illustrations of vertically travelling *S*-waves. Thick lines show exact VTSE and dotted lines show approximate VTSE.

Changing various values of δk, we can obtain accurate enough seismograms for a finite fault with $\delta k = 10^{-5}$ and express those seismograms as 'with VTSE' in the following figures. Since the amplitude of displacement spectra decreases in proportion to ω, for a finite fault (i.e. 26–28), the effect of VTSE decreases as frequency increases. This can be found in the expressions for I_L and I_W, (29) and (30). As a result, the effect of VTSE for the static component become important, as previous studies such as Hirata (1992) pointed out. Nevertheless, the discrepancy between exact VTSE and approximated VTSE is rather small in a very low frequency range even with $\delta k = 10^{-5}$. This is because their wavelengths are considerably larger than the depth of a finite fault, as schematically shown in Fig. 6. In summary, VTSE in a low frequency range has large energy in a finite fault case, but it can be approximated well with a small finite value of k, as illustrated in Fig. 6. We can obtain accurate seismograms including static displacement for a finite fault by adding $\delta k = 10^{-5}$ to horizontal wavenumbers without using

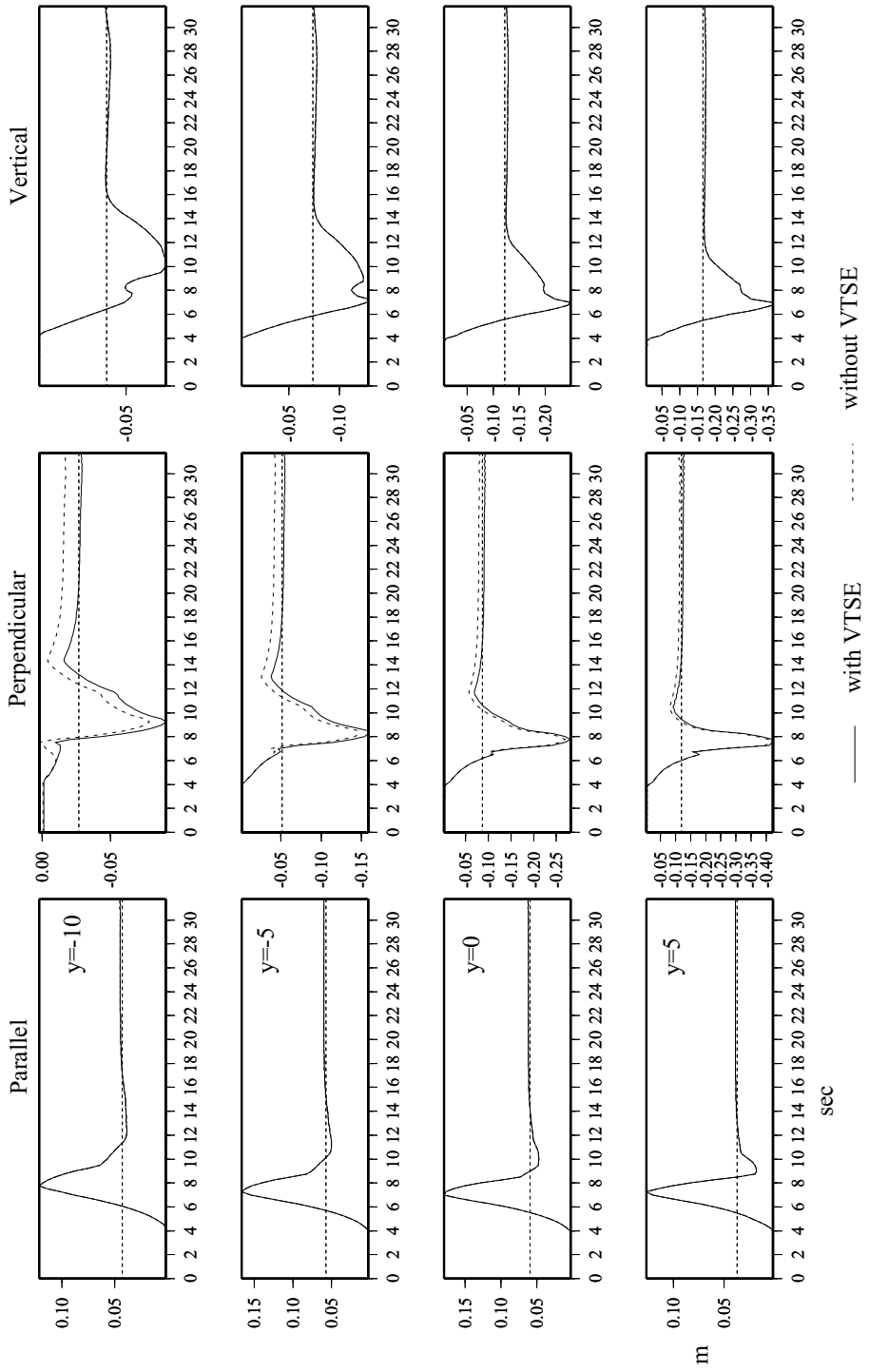

Figure 7. Comparison between synthetic seismograms with and without VTSE for a vertical dip-slip fault. Depth of fault top is 10 km. Station locations are shown in Fig. 4.

the special VTSE potential (15), which requires an additional procedure of the coordinate transform proposed by the previous studies for a point source.

As mentioned above, Hirata (1992) showed that the finite value of δk does not give satisfactory values for a point source. That is why VTSE has been dealt with a special potential scheme in Section 3. We found that a relatively large value of δk (i.e. 10^{-5}) can produce accurate seismograms for a finite fault without any special correction in the algorithm of the discrete wavenumber method. For a finite fault, the energy corresponding to VTSE (i.e. $k_x = k_y = 0$) is radiated only from a very small fraction of the fault at a given observation point. The majority of the energy comes from the other parts of the fault, so that a relatively large value of δk can give accurate seismograms for a finite fault.

Fig. 7 shows waveforms observed at stations above the fault, comparing those with and without VTSE. While an absolute value of the difference in static displacement is constant for all the stations, waveforms at a distant station without VTSE are largely distorted due to inaccurate static displacement, because of relatively small amplitude of seismograms there. Using the value of $\delta k = 10^{-5}$, that is, with VTSE in Fig. 7, we confirm that accurate seismograms of both dynamic and static displacement can be obtained. In the case of a vertical dip-slip fault, we obtain $\theta_s = 0$ from eq. (13). Since the displacement from VTSE is polarized, perpendicular to the fault strike, there is little difference in the parallel component between with and without VTSE at all the stations.

Fig. 8 shows synthetic seismograms for three fault models whose tops are at different depths. We can find that an absolute value of the difference in static displacement between with and without VTSE is almost the same as that of Fig. 7, regardless of fault depths. The energy of VTSE decreases with the fault depth, but its decreasing ratio is very small, as long as we consider a buried finite fault. In the case of $\omega = 0$, the energy of VTSE decreases as the depth of fault top increases in proportion to $\exp(\frac{-\omega_i z_o}{\beta})$ where ω_i is an imaginary part of angular frequency. Referring Bouchon & Aki (1977), we chose $\omega_i = \frac{\pi}{2T}$ in this study, where T is a duration of time window. Applying $T = 32$ (s), the amount of static displacement from VTSE is not more than 30 per cent of the entire seismograms for these fault models. It means that the attenuation by the effect of VTSE in space is slower than the attenuation of seismograms due to geometrical spreading. For this reason, the difference in seismograms between with and without VTSE must be large for a deep fault.

For a very shallow finite fault, waves with large horizontal wavenumbers should have the large amount of energy (e.g. Honda & Yomogida 2002), but the contribution of VTSE to surface displacement becomes relatively small. On the other hand, the contribution of VTSE becomes large as a fault is depth, because of the lack of the energy related to large wavenumbers.

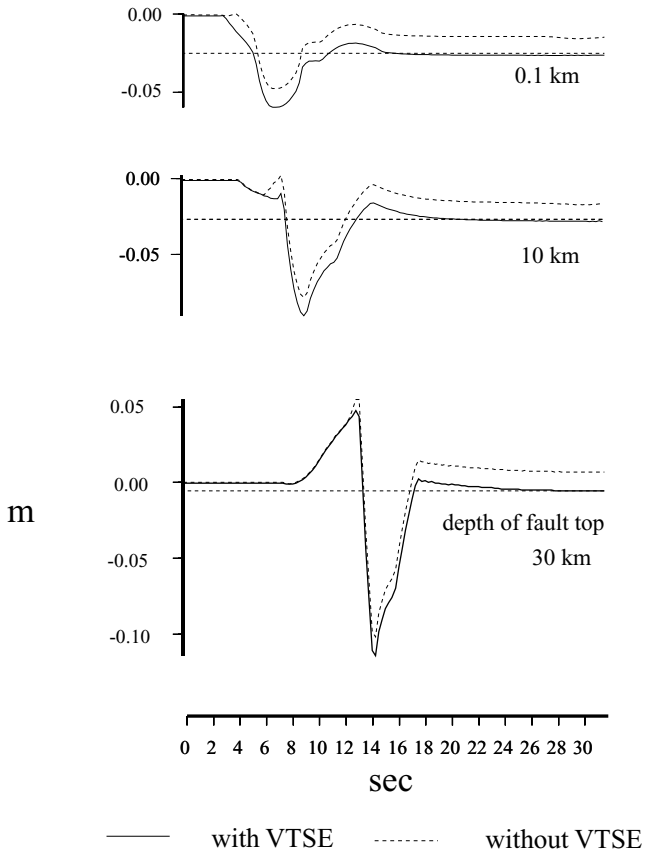

Figure 8. Same as Fig. 7 for faults with various depth. Horizontal component directing perpendicular of the fault strike of static displacements. The station is located at $y = -10$ km in Fig. 4.

6 CONCLUSIONS

We investigated the effect of VTSE, vertically travelling plane *S*-wave element, from a finite fault. Because of the singularity in the formulation originated from the finiteness of a fault, in addition to the singularity for a point source, we need to develop a new method to remove these singularities. Using a potential with an appropriately formulated fault finiteness term, we confirm that we can obtain accurate seismograms for both dynamic and static components, only by introducing a finite but not very small value of δk in stead of $k_x = k_y = 0$. We found that the difference between seismograms with and without VTSE is nearly constant at all the stations, implying nearly constant contribution of VTSE. Observed waveforms at a distant station appear to be largely distorted because of relatively small amplitude of seismograms there. For a shallow fault, the convergence in wavenumbers becomes very slow and the contribution of lager wavenumbers becomes relatively large (e.g. Honda & Yomogida 2002), while the contribution of VTSE (i.e. very small wavenumbers) does not depend on the top depth of a fault.

Together with our previous study (Honda & Yomogida 2002) on the problem of poor convergence in wavenumber domain, we can calculate surface displacements including the static component accurately in any finite fault accurately, simply by choosing 4 km^{-1} as the truncation number and the limiting number of 10^{-5} to horizontal wavenumbers k_x and k_y. Although we used a fault in a homogeneous half space, the above procedure and values can be applied to any layered media, which will be presented in another paper. Comparing synthetic seismograms proposed in this study with GPS or strong motion data, we will gain more quantitative estimations for fault processes than before.

ACKNOWLEDGMENTS

We wish to thank Prof. Junji Koyama for his valuable comments and checking our manuscript. We are deeply grateful to Dr Simon Tod and an anonymous reviewer for their valuable comments.

REFERENCES

Aki, K. & Richards, P.G., 1980. *Quantitative Seismology: Theory and Methods,* W. H. Freeman & Co., San Francisco.

Bouchon, M., 1979. Discrete wave number representation of elastic wave fields in three-space dimensions, *J. geophys. Res.,* **84,** 3609–3614.

Bouchon, M., 1981. A simple method to calculate Green's function for elastic layered media, *Bull. seism. Soc. Am.,* **71,** 959–971.

Bouchon, M. & Aki, K., 1977. Discrete wave-number representation of seismic-source wave fields, *Bull. seism. Soc. Am.,* **67,** 259–277.

Hirahara, K. *et al.*, 1996. GPS observations fo post-seismic crustal movements in the focal region of the 1995 Hyogo-ken nanbu earthquake -Static and real-time kenematic GPS observations, *J. Phys. Earth,* **44,** 301–315.

Hirata, K., 1992. Synthetic near-field seismograms due to rupture propagation fault models, *J. Phys. Earth,* **40,** 535–554.

Honda, R. & Yomogida, K., 1999. Synthetic Seismograms Near a Finite Fault System, *J. fac. Sci., Hokkaido Uni., geophys.,* **1.11,** 611–632.

Honda, R. & Yomogida, K., 2000. Accuracy of static displacement calculated by the discrete wave-number method, in *Abstract of Japan Earth and Planetary Science Joint Meeting,* Si005, The Joint Meeting Organization Office, Tokyo, 25–28 Jun., 2000.

Honda, R. & Yomogida, K., 2002. Static and dynamic displacement near a fault with the discrete wavenumber method, *Phys. Earth planet. Inter.,* in press.

Horike, M., Uebayashi, H. & Takeuchi, Y., 1990. Seismic response in three-dimensional sedimentary basin due to plane S wave incidence, *J. Phys. Earth,* **38,** 261–284.

Kennett, B.L.N. & Kerry, N.J., 1979. Seismic waves in a stratified half space, *Geophys. J. R. astr. Soc.,* **57,** 557–583.

Luco, J.E. & Apsel, R.J., 1983. on the Green's functions for layered half-space. part 1., *Bull. seism. Soc. Am.,* **73,** 909–929.

Ohori, M., Koketsu, K. & Minami, T., 1992. Seismic responses of three-dimensionally sediment-filled valleys due to incident plane waves, *J. Phys. Earth,* **40,** 209–222.

Okada, Y., 1985. Surface deformation due to shear and tensile faults in a half space. *Bull. Seism. Soc. Am.,* **75,** 1135–1154.

Takenaka, H., 1990. Theoretical Studies of Seismic wave fields in Irregularly layered media, in japanese, *PhD thesis,* Hokkaido University, Sapparo, Japan.

Uebayashi, H., Horike, M. & Takeuchi, Y., 1992. Seismic motion in a three-dimensional arbitarily-shaped sedimentary basin, due to a rectangular dislocation source, *J. Phys. Earth,* **40,** 223–240.

APPENDIX A: POTENTIALS IN THE CYLINDRICAL COORDINATE

To obtain formulations in the cylindrical coordinates from the Cartesian, we change variables by $k_x = k_r \sin(\theta' + \Phi)$, $k_y = k_r \cos(\theta' + \Phi)$, $x = r \sin(\Phi)$ and $y = r \cos(\Phi)$. r is the epicentral distance and k_r is the horizontal wavenumber. Φ and θ' are the azimuth of a receiver measured from the y (east) direction and the angle between the directions of the receiver and k_r, respectively (Fig. 2). The area element $dk_x dk_y$ is replaced by $k_r dk_r d\theta'$ over the whole horizontal wavenumber plane ($-\infty < k_x < \infty$; $-\infty < k_y < \infty$) being covered by the range of $0 \le k_r < \infty$ and $0 \le \theta' < 2\pi$. After some calculations for (2) ~ (4) (see, for example, Bouchon 1981), we obtain potentials in the form of Bessel functions $J_o(k_r r)$ and $J_1(k_r r)$:

$$\phi_{\pm} = \frac{i M_o}{8\pi^2 \mu k_\beta^2} \int_0^\infty \frac{k_r}{\nu} \left(A^0 J_0(k_r r) + A^1 J_1(k_r r) \right) \exp(\mp i \nu (z - z_o))\, dk_r \,, \tag{A1}$$

$$\psi_{SV\pm} = \frac{i M_o}{8\pi^2 \mu k_\beta^2} \int_0^\infty \left(B^0_{sv} J_0(k_r r) + B^1_{sv} J_1(k_r r) \right) \exp(\mp i \nu (z - z_o))\, dk_r \,, \tag{A2}$$

$$\psi_{SH\pm} = \frac{i M_o}{8\pi^2 \mu} \int_0^\infty \frac{1}{\gamma} \left(B^0_{sh} J_0(k_r r) + B^1_{sh} J_1(k_r r) \right) \exp(\mp i \nu (z - z_o))\, dk_r \,, \tag{A3}$$

where

$$A^0 = -k_r^2 \sin^2\Phi M_{xx} - k_r^2 \sin 2\Phi M_{xy} - k_r^2 \cos^2\Phi M_{yy} - \nu^2 M_{zz,} \tag{A4}$$

$$A^1 = -\frac{k_r}{r}\cos 2\Phi M_{xx} + \frac{2k_r}{r}\sin 2\Phi M_{xy} - \frac{k_r}{r}\cos 2\Phi M_{yy} \pm 2i\nu k_r(\sin\Phi M_{xz} + \cos\Phi M_{yz}), \tag{A5}$$

$$B^0_{sv} = \mp k_r^2 \sin^2\Phi M_{xx} \mp k_r^2 \sin 2\Phi M_{xy} \mp k_r^2 \cos^2\Phi M_{yy} \pm k_r^2 M_{zz,} \tag{A6}$$

$$B^1_{sv} = \mp\frac{k_r}{r}\cos 2\Phi M_{xx} \pm \frac{2k_r}{r}\sin 2\Phi M_{xy} \mp \frac{k_r}{r}\cos 2\Phi M_{yy} + \frac{k_r\left(k_\beta^2 - 2k_r^2\right)i}{\gamma}(\sin\Phi M_{xz} + \cos\Phi M_{yz}), \tag{A7}$$

$$B^0_{sh} = -\frac{k_r}{2}\sin 2\Phi M_{xx} + k_r \cos 2\Phi M_{xy} + \frac{k_r}{2}\sin 2\Phi M_{yy,} \tag{A8}$$

$$B^1_{sh} = \frac{1}{r}\sin 2\Phi M_{xx} - \frac{2}{r}\cos 2\Phi M_{xy} - \frac{1}{r}\sin 2\Phi M_{yy} \pm i\gamma(\cos\Phi M_{xz} - \sin\Phi M_{yz}) \tag{A9}$$

There are several integral representations of Bessel functions. To obtain our point source formulations in the cylindrical coordinate system, we use the following representations:

$$J_n(x) = \frac{1}{2\pi}\int_0^{2\pi} \exp i(x\sin\theta - n\theta)\,d\theta,$$

$$= \frac{1}{2\pi i^n}\int_0^{2\pi} \exp i(x\cos\theta + n\theta)\,d\theta,$$

and $J_{-n}(x) = (-1)^n J_n(x)$ where n is an integer. When n is extended to be real ν, another representation of Bessel functions is available with a Gamma function Γ as follows:

$$J_\nu(x) = \frac{1}{\pi^{\frac{1}{2}}\Gamma\left(\nu + \frac{1}{2}\right)}\left(\frac{x}{2}\right)^\nu \int_0^\pi \exp(ix\cos\theta)\sin^{2\nu}\theta d\theta\,.$$

In order to compare the potentials for a finite fault in Cartesian coordinates, we also consider a circular crack on a horizontal plane. Assuming that the crack grows at a constant velocity c until it stops at the final radius R and integrating point source potentials around the reference point in horizontal plane, Bessel functions in (A1), (A2) and (A3) are replaced by

$$J_o(k_r r) \Rightarrow \int_0^{2\pi} \exp(ik_r r\cos\theta')\frac{\exp iR\left(-k_r\cos\theta' + \frac{\omega}{c}\right)\left\{1 - iR\left(\frac{\omega}{c} - k_r\cos\theta'\right)\right\} - 1}{\left(-k_r\cos\theta' + \frac{\omega}{c}\right)^2}d\theta'\,, \tag{A10}$$

$$J_1(k_r r) \Rightarrow \int_0^{2\pi} \exp i(k_r r\cos\theta' + \theta')\frac{\exp iR\left(-k_r\cos\theta' + \frac{\omega}{c}\right)\left\{1 - iR\left(\frac{\omega}{c} - k_r\cos\theta'\right)\right\} - 1}{i\left(-k_r\cos\theta' + \frac{\omega}{c}\right)^2}\,d\theta'\,. \tag{A11}$$

In the formulations in the Cartesian coordinate, the fault finiteness terms (31) and (32) go to zero with the horizontal wavenumber $k_x = k_y = 0$. In contrast, the fault finiteness terms in above the formulations, (A10) and (A11), do not show this kind of problems even with $k_r = 0$ (Remember that the discrete wavenumber method introduces a small imaginary part of angular frequency). In the cylindrical coordinate, we can therefore deal with VTSE directly, using eqs (A10), (A11) and (15)–(25).